Effects of casting temperature on some properties of Co-Cr-Mo dental casting alloys

Håkon Herø
NIOM, Scandinavian Institute of Dental Materials, Oslo, Norway

Herø H. Effects of casting temperature on some properties of Co-Cr-Mo dental casting alloys. Acta Odontol Scand 1984;42:371–377. Oslo. ISSN 0001–6357.

The castability of three Co-Cr-Mo-C alloys, taken as the percentage of a grid pattern that was filled by metal, increased almost linearly from less than 10% to nearly 100% when the casting temperature was increased by 150°C. The surface finish became poor only at the highest applied casting temperature (1635°C). The ductility was significantly reduced by increasing the volume fraction of eutectic hard particles containing carbides. These particles cracked in a direction vertical to the stress in tensile tests, initiating a brittle failure. They also affected the work-hardening rate, and their volume fraction increased with the content of C and Cr. □ *Brittle fracture; carbides; castability; surface finish*

H. Herø, NIOM, Scandinavian Institute of Dental Materials, Forskningsveien 1, Oslo 3, Norway

Alloys based on Co, Cr, and Mo have for some time been used in dentistry to cast frameworks for partial denture restorations. Several properties of these alloys are of interest, such as: a) castability, which can be defined as the ability of the molten metal to fill the cavity of the mold; b) dimensional accuracy due to shrinkage during solidification and thermal contraction; c) the corrosion resistance; d) the surface finish; e) the yield point, which should be high to avoid plastic deformation when in use; and f) the ductility, which is of importance when the clasps are to be plastically bent to adjust their shape (1, 2).

The casting temperature is a variable that must be expected to affect many of these properties. It was the intention of this study to investigate the influence of temperature on castability, surface finish, and mechanical properties for three representative alloys with differences in chemical composition. The relationship between the mechanical properties and the structure was also examined.

Materials and methods

The three alloys investigated, their composition, approximate melting points, and codes are given in Table 1. The alloys were melted with Ar protection in an induction melting and centrifugal casting machine (Electromatic High Frequency Casting Machine, Howmedica, Inc.). The casting temperatures were checked with a radiation pyrometer and increased in steps of 15°C or 30°C until 120–135°C above the melting point. All wax patterns were invested in a phosphate-bonded material (Aurovest soft, BEGO, Bremer Goldschlägerei, Wilh. Herbst GmbH) preheated to 950°C, as recommended by the producer of the investment.

Two rod-shaped tensile specimens, 3 mm in diameter, with dimensions and spruing in accordance with the requirements of ISO/DIS 6871 for dental base metal casting alloys were made for each alloy and casting temperature. A standard wax was used for the patterns of the specimens (Blue Inlay Casting Wax, Regular, Type II, Sybron/Kerr Co.). Tensile testing (Wolpert Testatron, Wolpert Werkstoffprüfmaschinen GmbH) was carried out at a ram speed of 1.0 mm/min, using an extensometer with a gauge length of 10 mm.

The surface roughness, expressed as the centerline average R_A, was measured with a Perthometer (Type C5D, Dr.ing. Perthen GmbH) in the length direction on the spruing

Table 1. Alloy compositions in wt %*, melting point, and codes

Alloy	Code	Co	Cr	Ni	Mo	Mn	Fe	Si	C†	Sum	Approx. melting point, °C‡
Vitallium§	A	60	31	0.3	6.2	0.5	0.2	0.6	0.45	99.3	1425
Wironit¶	B	64	28	0.2	5.4	0.2	0.1	0.6	0.50	99.0	1480
Wironium¶	C	64	27	0.2	6.2	0.3	0.7	0.5	0.13	99.1	1480

* Soluble material analyzed by plasma-spectrographic method, non-soluble material by emission spectrometry.

† Determined by coulometric method after combustion to CO_2.

‡ Determined through separate experiments by putting a Pt/Pt Rh thermocouple with ceramic insulation into the melt. The melting point was taken as the temperature at which the alloy had properly melted.

§ Howmedica International Inc.

¶ BEGO, Bremer Goldschlägerei, Wilh. Herbst GmbH.

adjacent to the head of the tensile specimen after sand-blasting.

The castability was measured in accordance with a method developed by Whitlock et al. (3). The test pattern consisted of a polypropylene mesh screen (Small Parts, Inc.) 24 mm × 24 mm in area, having runner bars 2.0 mm in diameter along two adjacent edges and with a sprue attached to their junction, as shown in Fig. 1. The diameter of the threads in the mesh screen was 0.5 mm, and their spacing was 1.5 mm. The polypropylene sieve cloth was burned out in the same manner as wax patterns. The castability was measured by the fraction of the mesh screen that was filled by the liquid alloy during casting.

Metallographic samples were prepared by sectioning longitudinally half of the fractured tensile samples at each casting temperature for each alloy. Grinding and polishing were carried out with standard procedures. Finally, Al was evaporated on polished surfaces before they were examined in a combined microprobe and scanning electron microscope (SEM) (Cameca, type Camebax Microbeam). The fracture surfaces were also investigated with this instrument.

Vickers microhardness (10 g) on particles and matrix was measured on polished and etched heads of tensile specimens cast at high and low temperatures for each alloy (Table 2). The etchant consisted of 50 ml HCl, 50 ml H_2O, and 10 ml 3% H_2O_2. Six indentations were made on both particle and matrix in each sample. The volume fraction

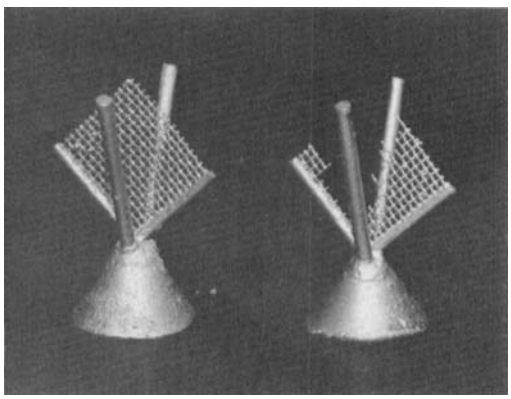

Fig. 1. The castability was measured by the fraction of a mesh screen filled by the molten metal.

Table 2. Vickers microhardness in kp/mm² of particles and matrix

Alloy	Casting temp., °C	Particle		Matrix	
		Mean*	SD	Mean*	SD
A	1455	661	301	306	69
	1525	709	112	288	68
	1605	515	170	370	47
B	1495	752	261	291	51
	1550	488	119	179	84
	1635	535	303	297	80
C	1495	499	93	233	64
	1550	323	139	271	23
	1635	578	253	361	119

* Average of six parallel measurements.

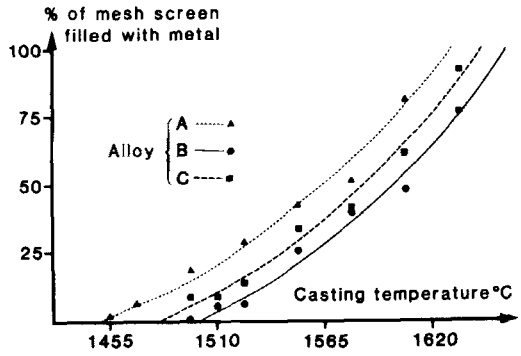

Fig. 2. Castability as a function of temperature for the three investigated alloys.

of particles was measured by the linear intercept method on SEM micrographs of polished and unetched samples.

Results

The percentage of the mesh screen filled by the molten metal as a function of casting temperature for the three alloys investigated is shown in Fig. 2. The castability increased almost linearly with temperature and approximately at the same rate for all three alloys.

The mechanical properties for the three alloys as a function of casting temperature are shown in Figs. 3, 4, and 5. The yield point $\sigma_{0.2}$ was between 600 and 650 MPa for all alloys independent of casting temperature. On the other hand, there was a substantial difference in total elongation. Alloy A had the poorest and alloy C the best ductility. No systematic effect of temperature on elongation could be observed. The average of σ_{UTS} was nearly the same for alloys A and B and somewhat lower for alloy C owing to a smaller work-hardening rate, as shown in Fig. 6. There was a tendency for σ_{UTS} to decrease with increasing temperature for all alloys. In Fig. 7 this is illustrated for alloy B by typical stress-elongation curves for a low and a high casting temperature.

The SEM investigations of the sectioned and polished tensile samples showed significant differences in the amount of particles formed between dendritic arms and at grain

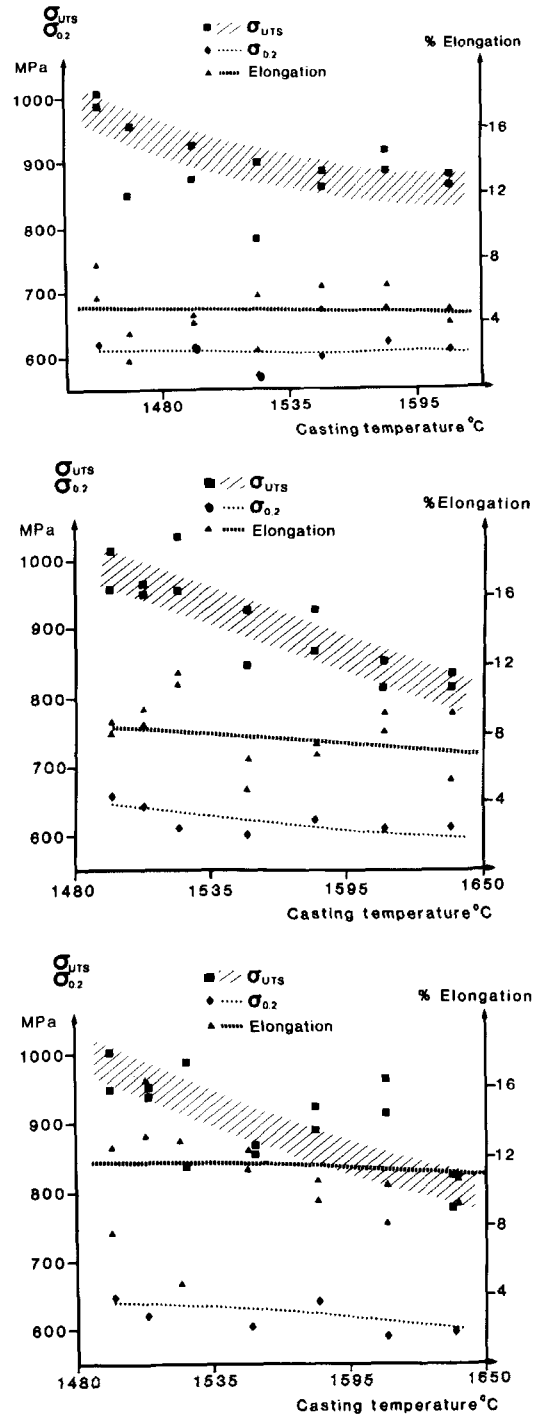

Figs. 3, 4, and 5. Mechanical properties measured by tensile testing as a function of casting temperature. Fig. 3 (top). Alloy A. Fig. 4 (middle). Alloy B. Fig. 5 (bottom). Alloy C.

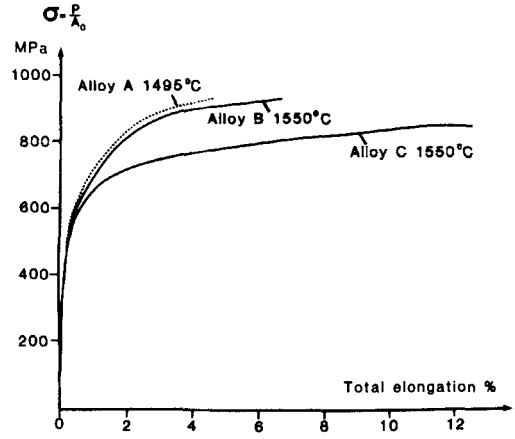

Fig. 6. Stress-elongation curves in tenstile testing for the three alloys cast about 50°C above their melting point.

boundaries. The alloys contained decreasing amounts in the following order: A, B, and C, as shown in Figs. 8, 9, and 10. By the linear intercept method the volume fractions were found to be 26%, 17%, and 14%, respectively. No systematic effect of the casting temperature on the structures could be observed.

The microhardness measurements showed that the particles were about twice as hard as the matrix. However, substantial scatter was observed (Table 2).

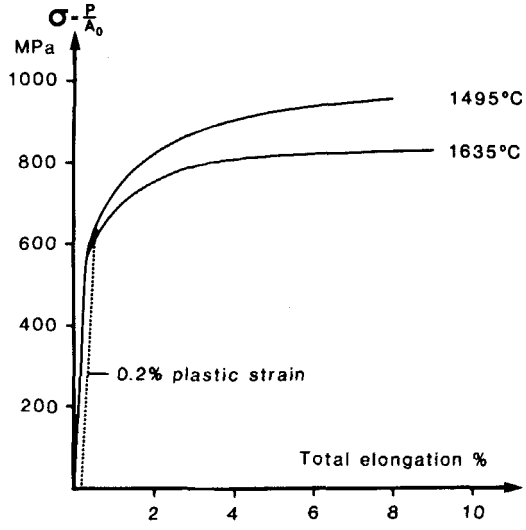

Fig. 7. Stress-elongation curves in tensile testing for alloy B at a low and high casting temperature.

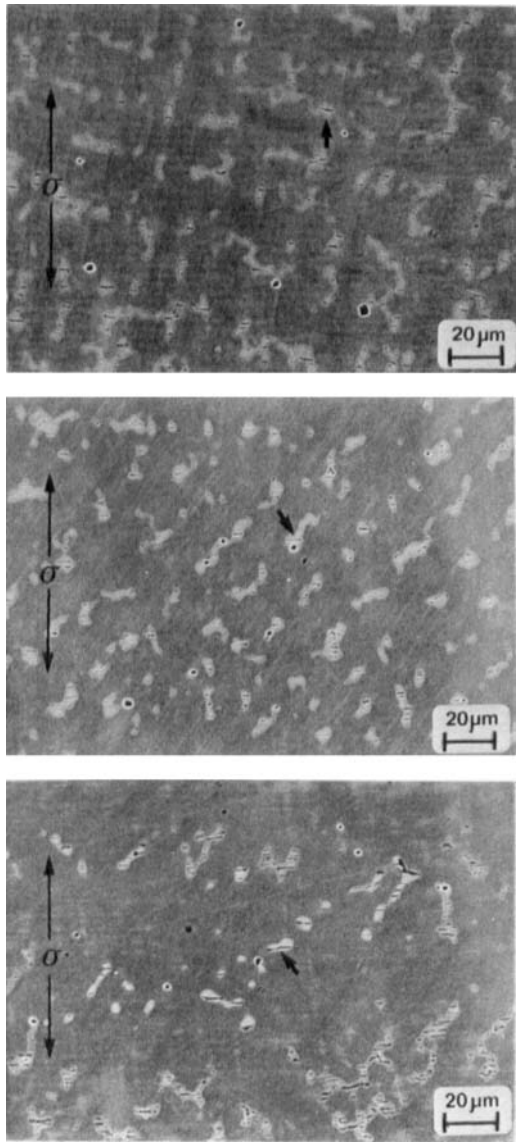

Figs. 8, 9, and 10. SEM micrographs (back-scattered electrons) of longitudinal cross-sections of tensile specimens adjacent to the fracture surfaces. Cracked particles indicated by arrow. Fig. 8 (top). Alloy A, cast at 1550°C. Fig. 9 (middle). Alloy B, cast at 1635°C. Fig. 10 (bottom). Alloy C, cast at 1580°C.

The results of the surface roughness measurements on the sprues as a function of casting temperature are given in Table 3. The average values of R_A were slightly better for alloy C than for alloys A and B. However, at the highest casting temperature (1635°C),

Table 3. Measurements of surface roughness determinant R_A in μm of the sprues for the investigated alloys

Casting temperature, °C	Alloy A	Alloy B	Alloy C
1455	1.43	—	—
1470	1.86	—	—
1495	1.87	1.14	1.49
1510	—	2.15	1.19
1525	2.17	1.62	1.56
1550	1.74	2.02	1.63
1580	1.75	1.76	1.49
1605	2.09	2.38	1.60
1635	—	3.70	5.70
Average values*	1.84	1.84	1.49
Standard deviation	0.24	0.43	0.16

* Measurements at 1635°C not included for alloys B and C.

which was used only for alloys B and C, a considerable surface deterioration was observed.

Discussion

Castability

The castability, measured by the percentage of complete cast segments of the sieve cloth pattern, increased almost linearly with the casting temperature, from less than 10% at the lowest applied casting temperature to close to 100% approximately 150°C above this temperature (Fig. 2). Only one casting was made at each temperature for each alloy, but the scatter in castability as a function of casting temperature for an alloy is reasonably small, so that the reproducibility seemed to be good and in accordance with previous experiments (3–5). The temperature measured by the radiation pyrometer was of course dependent on the emissivity coefficient of the melt. In the present measurements the melt was always covered by an oxide film, and the coefficient of emissivity could therefore be expected to remain reasonably constant with temperature for the present purpose. Furthermore, the method appeared to express well the expected improvement in fluidity (reciprocal of viscosity) with increasing temperature of the melt.

Fluidity, however, may not be quite the same as castability, which must be expected to be affected by other properties of the metal, like heat capacity and heat of fusion. Generally, the pure metals and alloys with a eutectic composition have been observed to possess the best castability (6).

It is interesting that the castability of the three investigated Co-Cr-Mo alloys increased with the temperature at approximately the same rate (Fig. 2). The approximate melting point of alloy A was about 50°C lower than that of alloys A and B, which can be explained by its higher Cr content in a view of the ternary Co-Cr-C phase diagram (7).

Relationship between mechanical properties and structure

The particles illustrated in Figs. 8, 9, and 10 for alloys A, B, and C, respectively, have previously been observed by transmission electron microscopy (TEM) to be mainly eutectic, with thin (0.1–0.2 μm) alternating lamellae of $M_{23}C_6$ (M = Cr and Mo) and the Co-rich fcc phase (8). They are located either interdendritically or at grain boundaries. The segregation of C, Cr, and Mo was substantial. The intensity of back-scattered electrons increased with the atomic number of the elements, so that Mo and C tended to make the appearance bright and dark, respectively. However, the particles could also be more complex and, in addition, consist of other phases, possibly $Cr_{7-x}Co_xC_3$. In any case, these particles had a flow stress approximately twice as high as the Co-rich fcc matrix, to judge by the microhardness measurements (Table 2). During the plastic deformation in the tensile test considerable and increasing elastic stresses were built up in the particles because of coherence with matrix (8) and plastic incompatibility. Finally, the stresses in the particles reached a level at which they cracked. Quite a few fractured particles were observed adjacent to the fracture surface in the present materials (Figs. 8, 9, and 10). Typically, these cracks ran across the particles and vertical to the tensile axes. The SEM micrographs of fracture surfaces frequently revealed a dendritic pattern of particles (Fig. 11). In brittle materials cracked particles can

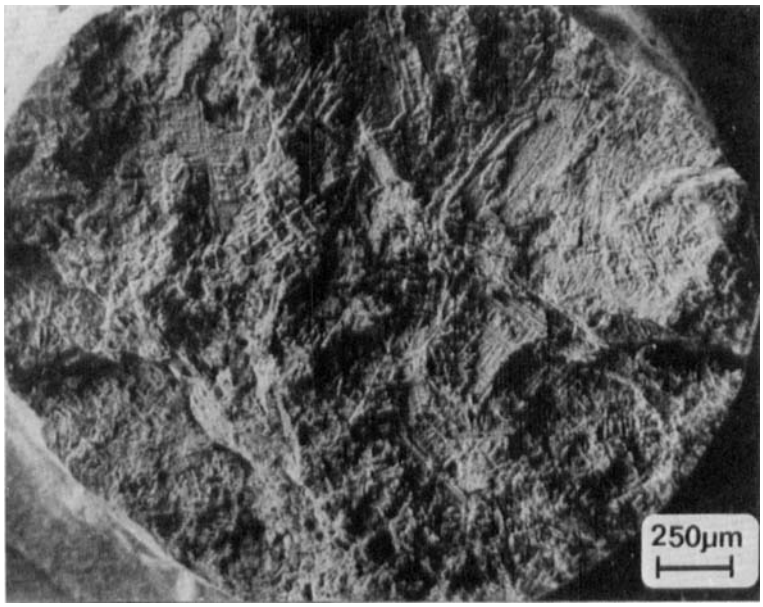

Fig. 11. SEM micrograph of the fractured surface of a tensile specimen alloy A, showing a dendritic pattern of particles.

initiate rapid fracture propagation, and the fracture stress σ_F in plane stress in the material containing a crack of length c can be expressed as follows according to the Orowan-Irwin equation (9):

$$\sigma_F = \frac{E(2\gamma + \gamma_p)}{\pi c},$$

where E is the elastic modulus, γ the surface energy, and γ_p the plastic work in front of the propagating crack tip. In metallic materials γ_p usually dominates over γ. Depending on the characteristic γ_p value for the material being tested and the length of a created crack, brittle failure occurs as soon as σ_F reaches a critical value.

In this respect the volume fraction of hard particles is of importance in three ways: 1) They cause a rapid work-hardening rate and increased flow stress for several reasons (10). The higher the volume fraction of hard, coherent particles, the steeper is the initial plastic part of the load-elongation curves, as shown in Fig. 6 for alloys A, B, and C, cast approximately 50°C above their melting points. The hardness of the particles will also affect the work-hardening rate, but no statistically significant differences between the alloys were observed (Table 2). 2) A high volume fraction and a correspondingly large tensile stress imply that the chance for a particle to crack for a given strain will also increase, provided the fracture stress of the particles themselves are unchanged. 3) A high volume fraction of particles will most likely create a path for easy crack propagation and thus a low value of γ_p.

Alloys A, B, and C have been found to contain decreasing amounts of particles (26%, 17%, and 14%, respectively) owing to different contents of C, Mo, and Cr. These are higher fractions than what has been found in the same alloys previously on unetched light optical micrographs (8). This discrepancy is probably due to better contrasts, so that more particles become visible in the present SEM micrographs. However, the ranking of the alloys remains the same. Thus the observed average levels of elongations (4%, 7%, and 12%, respectively, in Figs. 3, 4, 5) can readily be explained.

Some scatter in the observed total elongation as a function of casting temperature and within two parallel specimens can be observed. This is reasonable because the elongation can be expected to depend on the

strain necessary to produce a cracked particle of a critical size, which again is influenced by local stress concentrations and the orientation of the particle relative to the applied tensile stress. Furthermore, occasional casting defects may influence the strain to fracture. No systematic variation in ductility and volume fraction of particles with casting temperature could be detected for any of the three alloys.

In view of the scatter in elongations, incidental variations in the tensile strength values can also be expected, since the tensile load increases with strain. Only a band of tensile strengths is therefore indicated in Figs. 3, 4, and 5. In spite of this scatter, some difference among the alloys was shown with regard to σ_{UTS}. This indicated by the stress-strain curves in Fig. 6, where the ultimate tensile strength for alloys A and B is higher than for alloy C, mainly due to the higher work-hardening rate because of the larger volume fraction of particles. On the other hand, the elongation to maximum load at which fracture occurred in the present materials is considerably larger for alloy C. Thus the increase in stress takes place over a greater range of strain. The net effect is that σ_{UTS} is only marginally smaller for alloy C than for alloys A and B, as shown in Figs. 3, 4, and 5. Another important feature in these curves is the tendency for σ_{UTS} to become smaller with increasing casting temperature. In particular, this seemed to be the case for alloy B, and Fig. 7 shows typical stress-strain curves for this alloy at a high and low casting temperature. More work is needed to explain this difference in work hardening, since the present investigations did not disclose structural changes of importance for this property as the casting temperature increased. The only structural feature that appeared to be dependent on temperature was an increase in grain size and dendrite arm spacing with temperature. Such a relationship indicates a decreased cooling rate (6), which is likely to occur with increasing temperature of the melt. However, structural details such as phases, thickness of lamellae in eutectics, and particles precipitated in the solid state can only be observed by TEM.

Surface finish

The centerline average values for alloy C ($R_A = 1.49$) excluding the highest casting temperature (1635°C) were slightly better than those for alloy A ($R_A = 1.84$). Student's *t* test showed this difference to be above the 5% significance level when using the standard deviations in Table 3. However, the same numeric difference between the average values of R_A for alloys B and C was not statistically significant. It is interesting that only the highest casting temperature (1635°C) produced a substantially coarser surface finish (Table 3), which also could be observed by visual inspection. The surfaces were sandblasted before the Perthometer measurements, and the materials may have responded differently to this treatment. However, the substantial increase in surface roughness for the highest casting temperature is more likely to be due to increased reactions of the melt with the mold walls.

References

1. Craig RG. Restorative dental materials. 6th ed. St. Louis, Mo., The C.V. Mosby Co., 1980:327.
2. Phillips RW. Skinner's science of dental materials. 8th ed. Philadelphia, Pa., The W.B. Saunders Co., 1982:547.
3. Whitlock RP, Hinman RW, Eden GT, Tesk JA, Dickson G, Parry EE. A practical test to evaluate the castability of dental alloys [IADR abstract 374]. J Dent Res 1981;60(special issue A):404.
4. Agarwal DP, Ingersoll CE. Evaluation of various castability patterns by comparison with practical castings [IADR abstract 1502]. J Dent Res 1982;61:345.
5. Hinman RW, Tesk JA, Whitlock RP, Parry EE, Durkowski JS. Use of a castability test for optimizing mold and casting temperature [IADR abstract 1361]. J Dent Res 1982;61:329.
6. Flemings MC. Solidification processing. New York, N.Y.: McGraw-Hill Book Co., 1974;144,222.
7. Köster W, Sperner F. Das Dreistoffsystem Kobalt-Chrom-Kohlenstoff. Arch Eisenhüttenw 1955;26:555–9.
8. Herø H, Syverud M, Gjønnes J, Horst JA. Ductility and structure of some cobalt-base dental casting alloys. Biomaterials 1984;5:201–8.
9. Knott JF. Fundamentals of fracture mechanisms. London: Butterworths, 1973:110.
10. Speich GR, Miller RL. Mechanical properties of ferrite-martensite steels in structure and properties of dual-phase steels. In: Kot RA, Morris JW, eds. Proceedings of the Symposium by The Metallurgical Society of AIME. New Orleans, La.: 19–21 February 1979:169.

Received for publication 2 February 1984